IEEE Access
Multidisciplinary | Rapid Review | Open Access Journal

Received April 20, 2019, accepted May 13, 2019, date of publication May 16, 2019, date of current version May 30, 2019.

Digital Object Identifier 10.1109/ACCESS.2019.2917267

Detection of Subtle Bruises on Winter Jujube Using Hyperspectral Imaging With Pixel-Wise Deep Learning Method

LEI FENG, SUSU ZHU, LEI ZHOU, YIYING ZHAO, YIDAN BAO, CHU ZHANG, AND YONG HE

College of Biosystems Engineering and Food Science, Zhejiang University, Hangzhou 310058, China
Key Laboratory of Spectroscopy Sensing, Ministry of Agriculture and Rural Affairs, Hangzhou 310058, China

Corresponding author: Chu Zhang (chuzh@zju.edu.cn)

This work was supported in part by the National Key Technologies R&D Program of China under Grant 2018YFD0101002, and in part by the National Natural Science Foundation of China under Grant 31471417.

ABSTRACT Winter jujubes get bruised easily during harvest and transportation. In order to detect subtle bruises on winter jujubes in a more efficient way, a rapid and accurate technique, hyperspectral imaging was used. Near-infrared reflectance (NIR) and visible/near-infrared reflectance (Vis-NIR) hyperspectral imaging at the spectral region of 874-1734 nm and 380-1030 nm, respectively, were applied in this study. The hyperspectral images of winter jujubes from four geographical origins were acquired. Pixel-wise spectra were extracted and preprocessed; pixel-wise principal component analysis (PCA) was used to conduct a qualitative analysis. Accuracy, true positive rate (TPR) and false positive rate (FPR) were utilized to compare the efficiency of the models. Support vector machine (SVM), logistic regression (LR) and a deep learning method, and convolutional neural network (CNN) were used to build pixel-wise classification models based on single or all geographical origins for quantitative analyses. All the models using NIR spectra obtained decent results with accuracies in the range of 90–100%, and TPRs and FPRs close to 1 and 0, respectively. Compared with the other two methods using Vis-NIR spectra, the CNN model based on all geographical origins got the best performance with most of the accuracies surpassing 85%. For Vis-NIR spectra and NIR spectra, the overall time efficiency for modeling and prediction of CNN was at an intermediate level among the three models. The short prediction time of CNN indicated that CNN had the potential for real-time detection. The prediction maps obtained by the CNN models indicated that the color information and geographical origins could affect the detection performance. The overall results demonstrated the promising potential for detecting subtle bruises on winter jujubes using pixel-wise spectra extracted from the hyperspectral images at the two spectral ranges with the deep learning method. The results in this study would help to develop an online winter jujube bruises detection system in the future.

INDEX TERMS Winter jujubes, hyperspectral imaging system, support vector machine, logistic regression, convolutional neural networks.

I. INTRODUCTION

Winter jujube is one of the most favored fruits in China due to its good taste and abundant nutrition. The winter jujube is harvested and stored at a low temperature. The ripen winter jujube becomes browning and softening and its quality deteriorates after harvesting [1]. Bruises are the damage to the soft tissue of fruit caused by external forces, which can cause physical changes in the texture of the fruit as well as chemical changes in color, odor and taste [2]. It is a common knowledge that winter jujubes often suffer from mechanical defects during gathering, transportation and postharvest treatment. As time goes by, the bruise can develop into mildew or decay, which not only affects the quality of bruised winter jujubes, but also has chances to infect other healthy winter jujubes.

Traditionally, discriminating bruised winter jujubes is performed by human naked eye, which is inefficient and toilsome for large-scale processing and production. At present, to meet the requirement of industrial development, some

The associate editor coordinating the review of this manuscript and approving it for publication was Jon Atli Benediktsson.

non-destructive methods are applied to evaluating fruit attributes. Cox et al. utilized electrical impedance measurements to detect and monitor the development of the bruises on apples named 'Granny Smith'. The results showed that impedance measurements could distinguish bruises of different level in apples successfully [3]. Zhang et al. employed electronic nose to establish quality indices model for pears. All models presented good prediction results for firmness and soluble solid content [4]. Some studies detected apple bruises using machine vision technology. Combined with certain image processing algorithm, early bruises on apples could be detected successfully [5], [6].

In addition to the methods mentioned above, hyperspectral image technology is a non-destructive testing method which combines image technique and spectroscopy technology [7]–[10]. Hyperspectral imaging technology can obtain the chemical information of heterogeneous samples and further explore the spatial distribution of chemical components [11], [12]. In recent years, the hyperspectral technology has been extensively used in the detection of fruit bruises. Baranowski et al. (2012) used a hyperspectral system to detect bruises in apples. Otsu thresholding algorithm was used to distinguish bruised areas. It showed that the bruised tissue could be distinguished using principal components analysis (PCA) and minimum noise fraction (MNF) analysis methods [13]. Zhao et al. (2010) also used PCA to extract useful information for bruise detection on pears [14]. Fan et al. (2017) successfully detected bruises of blueberry using near-infrared reflectance (NIR) hyperspectral reflectance imaging with optimum wavelengths selected by competitive adaptive reweighted sampling (CARS) [15]. Then the same team discriminated bruises of blueberry using two hyperspectral imaging systems, which demonstrated the possibility of blueberry bruises detection using the data fusion strategy [16]. Gamal et al. (2007) selected three effective wavelengths in the near infrared region to detect early bruises of apples. An adaptive thresholding was used to identify bruised areas of apples. The results showed the possibility of the detection of apple bruises after 1 h using hyperspectral imaging technology [17].

Among the studies detecting fruit bruises based on hyperspectral imaging, the object-wise analysis based on regions of interest (ROI) is a common method used for normal and bruised areas selected [18]–[20]. However, the ROIs for normal and bruised area were selected manually. The hyperspectral reflectance variation caused by the height differences of the sample surface was also ignored by analyzing spectral data within ROIs [21]. The object-wise analysis is a common feature extraction method which uses average spectra of samples for data analysis. Although it can save time for modelling, it still loses the detailed information of samples [22]–[24]. The pixel-wise analysis uses spectra of individual pixels of samples for analyses. Compared with the object-wise analysis, the pixel-wise analysis contains much more detail information, though it will take more time for data processing. Studies have showed that pixel-wise spectra are effective in hyperspectral image analyses [8], [21], [25]. Che et al. (2018) used pixel-wise spectra extracted from hyperspectral images of bruised apples to detect apple bruises. The overall results showed the potential for bruised region extraction based on pixel-wise hyperspectral imaging [26].

How to deal with the large amount of pixel-wise spectra is a great challenge at present. Deep learning, a new field in artificial intelligence, has been one of the hottest fields in artificial intelligence, due to its characteristics such as feature representation, self-learning and effectiveness of dealing with large data, etc [27], [28]. Deep learning has been popularly applied in various fields, and has shown competitive or better performances compared with other machine learning methods [29]–[32]. The hyperspectral image analysis is a hot application area of the deep learning. Researchers have conducted a large number of studies to use deep learning in hyperspectral images of remote sensing [33]–[35]. Only a few researchers have introduced deep learning in spectral data analysis and ground-based hyperspectral images [36]–[39]. These studies indicate that deep learning has great potential in spectral data and hyperspectral image analyses.

This study used hyperspectral imaging systems at two different spectral ranges to detect bruises in winter jujubes. Winter jujubes from different geographical origins were studied. Detection performances varied with geographical origins, indicating the influence of geographical origins of winter jujubes. Pixel-wise spectra were extracted for analyses, and the results showed that it was feasible to use pixel-wise spectra for bruise detection of winter jujubes. Better detection performances were obtained by near-infrared hyperspectral imaging, and the results showed that NIR spectra would be better for the winter jujube bruise detection for industry applications. More importantly, convolutional neural network (CNN) was adopted to detect winter jujube bruises along with traditional methods support vector machine (SVM) and logistic regression (LR). Detection performances of CNN were close to SVM and LR. Time efficiency of modelling and prediction showed that CNN had great potential for real-time detection. The results of this study would help researchers from related fields to use deep learning methods for the similar tasks on the other fruits, and extend the use of the deep learning in the hyperspectral image analyses for food and the other fields.

II. MATERIALS AND METHODS

A. SAMPLES PREPARATION

Winter jujubes (Zizyphus Jujuba Mill.) from four different geographical origins were collected during the harvest period in 2017, including Dali, Shanxi Province, China; Huanghua, Hebei Province, China; Linyi, Shanxi Province, China; Zhanhua, Shandong Province, China, respectively. For the 4 geographical origins, 150 samples of single geographical origin were prepared, including 75 healthy jujubes and 75 bruised jujubes. The bruises in winter jujubes were mainly

caused by external force during the process of picking and transportation, and the region of bruised winter jujube samples were marked for the convenience of spectral data extraction. All jujubes were washed, dried and stored at room temperature of 20 °C for 24 hours for hyperspectral image acquisition.

B. HYPERSPECTRAL IMAGING ACQUISITION

1) HYPERSPECTRAL IMAGING SYSTEM

In order to acquire hyperspectral images, a NIR hyperspectral imaging system with the spectral range of 874-1734 nm and a Vis-NIR hyperspectral imaging system with the spectral range of 380-1030 nm was applied to this experiment.

The Vis-NIR hyperspectral imaging system consists of an imaging spectrograph (ImSpector V10E; Spectral Imaging Ltd., Oulu, Finland) with the spectral resolution of 2.8 nm, a high performance CCD camera (Hamamatsu, Hamamatsu City, Japan) with 672 × 512 (spatial × spectral) pixels and a camera lens (OLES23; Specim, Spectral Imaging Ltd., Oulu, Finland).

NIR hyperspectral imaging system comprised an imaging spectrograph (ImSpector N17E; Spectral Imaging Ltd., Oulu, Finland), a high performance camera (Xeva 992; Xenics Infrared Solutions, Leuven, Belgium) with 326 × 256 (spatial × spectral) pixels and a camera lens (OLES22; Specim, Spectral Imaging Ltd., Oulu, Finland).

A platform integrated the two systems. For the platform, two 150 W tungsten halogen lamps (3900 Lightsource, Illumination Technologies Inc., USA) are used for illumination; a conveyer belt driven by a stepper motor (Isuzu Optics Corp., Taiwan, China) is used for sample motion. Hyperspectral image acquisition was controlled by corresponding softwares (Spectral Image-V10E and Spectral-Image-Xenics 17E, Isuzu Optics Corp., Taiwan, China), which could be applied to calibrating and analyzing the hyperspectral images.

To prevent hyperspectral images distortion and get distinct hyperspectral images, three parameters, including moving speed of conveyer belt, the exposure time and the height between the lens of the camera for NIR hyperspectral imaging system, were set as 15 mm/s, 3 ms and 19.5 cm, respectively. For the Vis-NIR hyperspectral imaging system, three of the same parameters were adjusted to 2.2 mm/s, 0.05 s and 19.5 cm.

2) HYPERSPECTRAL IMAGE ACQUISITION AND CALIBRATION

The raw hyperspectral images should be corrected into reflectance images by the following equation for further analysis:

$$I_c = \frac{I_{raw} - 1_{dark}}{I_{white} - I_{dark}} \quad (1)$$

where I_c represented the calibrated image; I_{raw} represented the raw image; I_{dark} is the dark reference image acquired by covering the lens with lens cap whose reflectivity is about 0%; I_{white} is the white reference image collected using a piece of pure white Teflon board whose reflectivity was about 100%.

C. SPECTRAL EXTRACTION AND PREPROCESSING

After image correction, spectral information could be extracted from preprocessed hyperspectral images. For healthy sample, the entire sample region in the hyperspectral-image was defined as the region of interest (ROI) and all the pixel-wise spectra within the ROI were extracted. It was noted that some regions were over exposed, and these pixels were removed during pixel-wise spectra extraction. For bruised sample, the mask procedures on binary image couldn't be used to distinguish the bruised area on winter jujubes automatically. Thus, a rectangle area in the center of the marked area (Figure 1) were manually defined as the ROI, and all the pixel-wise spectra within the ROI were extracted. It should be noted for the bruised samples, only one bruised region was marked, and there might be more bruised regions within the bruised samples. To reduce the influence of unflatten surface of different ROIs, the normalization preprocessing on the extracted spectra was applied. More importantly, it could be observed in Figure 1 that the marked bruised regions had similar color as some healthy regions. The similarity in color of bruised regions to healthy regions made it difficult to detect bruises visually.

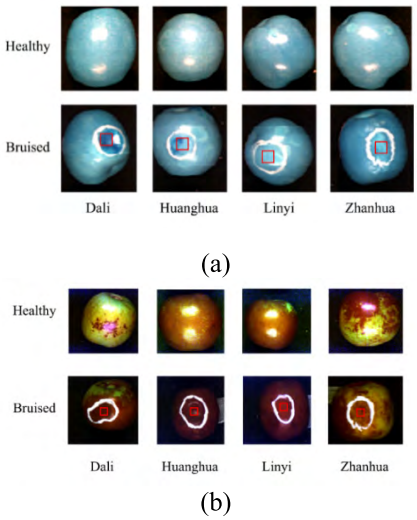

FIGURE 1. Hyperspectral images of (a) NIR; (b) Vis-NIR. (Red boxes in the images were selected as the region of interest of bruised samples.)

The beginning and the end part of the spectral data included obvious noises, so the spectral range of 975-1646 (200 wavelengths) nm for the NIR hyperspectral images and 502-947 nm (350 wavelengths) for the Vis-NIR hyperspectral images were used for further analyses. For both NIR and Vis-NIR hyperspectral images, the original pixel-wise spectra was denoised by wavelet transform (WT) basis function using Daubechies 8 (db8) with decomposition level 3. After WT denoising, an area normalization preprocess was applied on the pixel-wise spectra to reduce the influence of light intensity variations caused by fruit shape [40]–[42].

D. DATA ANALYSIS METHODS

1) PRINCIPAL COMPONENT ANALYSIS

Principal component analysis (PCA), a multivariate statistical method, is commonly used for data dimension reduction by studying the correlation between multiple variables. The first few principal components (PCs) contained the most spectral information of samples, so the first few PCs can be used to explore the differences among samples. As for hyperspectral image, PCA can be conducted on pixels to form pixel-wise score images [43], [44]. PCA was applied to explore qualitative discrimination of healthy and bruised winter jujubes in this study.

2) SUPPORT VECTOR MACHINE

Support vector machine (SVM) is a generalized linear classifier based on supervised learning method used for data classification and regression. SVM is one of the most commonly used and best-performing classifiers, which can usually get better results than other algorithms on small sample training sets. SVM Radial basis function (RBF) is a widely used kernel function for SVM models in spectral data analysis [45], [46]. The regularization parameter c and kernel function parameter g are two main parameters which should be decided for SVM models. In this study, grid-search was applied in SVM models optimization. The values of regularization parameter c and kernel function parameter g of SVM models with the highest accuracy were chosen as the optimal model parameters. SVM is conducted on Matlab R2017a (The Math Works, Natick, MA, USA) [47], [48].

3) LOGISTICAL REGRESSION

Logistic regression (LR) is a common method for dealing with the problem of binary classification [49], as well as the most popular algorithm for solving problems in industrial scale. What's more, LR is easy to understand and implement with simple formula and low computational burden. The dependent variable of a binary logistic model has two possible values labeled "0" and "1". Based on linear regression model, sigmoid function is added to map the linear combination of independent variables into the value in range [0, 1].

In this research, we fit the LR model utilizing the generalized linear model regression toolbox of Matlab R2017a (The Math Works, Natick, MA, USA).

4) CONVOLUTIONAL NEURAL NETWORK

Convolutional neural network (CNN) studies local patterns from original data based on local sparse connections, and it can reduce the risk of overfitting by weight sharing [50].

As shown in Figure 2, we designed a simple CNN architecture consisting of two main blocks utilizing MXNet1.4.0 (MXNetAmazon, Seattle, WA, USA) [51].

The first block is convolutional block including two convolutional layers, each followed by a max pooling layer and an activation layer. Considering that the inputs are one-dimensional vectors composed of pixel-level spectral

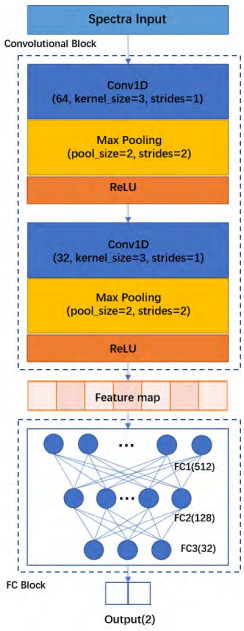

FIGURE 2. The architecture of CNN.

data, we adopt one-dimensional convolution (Conv1D) [38]. The parameters in CNN were chosen by empirical method at first. In order to find the optimal architecture of the CNN models, the parameters were adjusted according to the accuracy of the validation set and the simplicity of the model. All convolutional layers in the proposed model use a kernel size of 3, stride of 1 without padding. The number of filters is 64 for the first convolutional layer and 32 for another one. The convolutional block can be trained by pixel-level spectra to extract abstract spectral features. The second block is a fully connected (FC) network consisting of three layers of neural networks, each of which contains 512, 128, 32 neurons respectively. And we add a dense layer at last for output. Features extracted by the convolutional block was fed into the FC block to predict the health status.

Furthermore, the proposed architecture used the rectified linear unit (ReLU) as activation function. The output of the CNN model is followed by a softmax function to convert the output data of the last dense layer to a value in the range of [0, 1] as classification confidence scores. Cross entropy cost function, which calculates the expected value of the loss for a distribution over outcomes, was chosen as the loss function.

The training procedure was performed by optimizing the softmax cross entropy loss using the SGD algorithm. The learning rate (L_0) was reduced with the increase of training epoch according to the following equation:

$$L = \frac{L_0}{1 + kt} \tag{2}$$

where L denotes the initial learning rate; t is the number of epochs; and k is set to 0.001 in this research which determines the speed of reduction. Other hyperparameter of the CNN is shown in Table 5 and Table 6.

The Pseudocode of the Method was as Follows:

Data preprocessing
Input: raw pixel-level spectra data S of m bands by n samples
Function Area normalization:
  For each s(m×1) in S:
    s = s./sum(s)
  end For
mark the new S as S'
output: S' and divide S' as S'_calibration, S'_validation, S'_prediction
Training task
Input: a batch of preprocessed pixel-level spectra data of m bands
Define the network architecture as net() and set the trainer using MXNET
ctx=gpu(0)
  (0): Conv1D(64, kernel_size =3, stride =1, Activation(relu))
  (1): MaxPool1D(size =2, stride =2,)
  (2): BatchNorm(eps =1e-05, momentum =0.9)
  (3): Conv1D(32, kernel_size =3, stride =1, Activation(relu))
  (4): MaxPool1D(size =2, stride =2,)
  (5): BatchNorm(eps =1e-05, momentum =0.9)
  (6): Dense(512, Activation(relu))
  (7): BatchNorm(eps =1e-05, momentum =0.9)
  (8): Dense(128, Activation(relu))
  (9): BatchNorm(eps =1e-05, momentum =0.9)
  (10): Dense(32, Activation(relu))
  (11): BatchNorm(axis =1, eps =1e-05, momentum =0.9)
  (12): Dense(2, linear)
For epoch = 1 to defined_epochs:
    start = time()
    learning rate = init_learning_rate/(1+k *epoch)
For each batch in S'_calibration as [Xi, yi]:
      loss = softmax cross entropy loss
      ($\hat{y}$ =net(Xi),yi)
    net.backward()
  calculate calibration_accuracy
  calculate validation accuracy
  print(epoch, loss, calibration accuracy, validation accuracy, time() - start))
End For
Testing task
Load the trained network
For each batch in S'_prediction as [Xi, yi]:
    $\hat{y}_{test}$ (the ith batch) = net(Xi)
calculate prediction_accuracy
Visualization
Load a spectral image I in shape of a*b*m
Load the trained network
$\hat{y}$ = net(For each pixel in I)
Reshape $\hat{y}$ as a*b
plot the colormap

5) CALIBRATION SET SELECTION

In this study, pixel-wise spectra of healthy jujubes were extracted from the entire sample region, whereas pixel-wise spectra of bruised samples were extracted from the marked ROIs. The number of pixel-wise spectra of healthy samples was much larger than that of bruised regions. Thus similar number of representative pixel-wise spectra was selected from the original healthy pixel-wise spectra.

To select representative pixel-wise spectra, the following procedures were conducted:

1) Calculate the average spectrum of all healthy pixel-wise spectra as reference spectrum;
2) Use spectral angle mapping (SAM) to calculate the spectral angle value between each pixel-wise spectra and the reference spectrum;
3) Rank the pixels according to the spectral angle value from low to high. The pixel-wise spectra with the lowest and highest spectral angle values were firstly selected into the calibration set;
4) Divide the remaining samples uniformly into the certain number of groups according to the spectral angle value. Pixel with medium spectral angle value of each group was selected into the calibration set. Note that there might be empty groups, the corresponding samples were not chosen, resulting in less selected pixels. Thus the number of groups to be divided should be larger than the expected selected number.

6) RECEIVER OPERATING CHARACTERISTICS

Receiver operating characteristics (ROC) is used to illustrate the discrimination ability of a binary classifier system.

True Positive (TP), False Positive (FP), True Negative (TN) and False Negative (FN) are terminologies used in the description of ROC.

TP means the classified result and the actual label are both positive. FP means the classified result is positive while the actual label is negative. TN means the classified result and the actual label are both negative. FN means the classified result is negative while the actual label is positive.

In this study, the label ''healthy'' was defined as positive and label ''bruised'' was defined as negative.

True positive rate (TPR) and false positive rate (FPR) are features introduced by Fawcett (2004) to evaluate the performance of the classifier. The equations are presented as follows [52]:

$$TPR = \frac{TP}{TP + FN} \tag{3}$$

$$FPR = \frac{FP}{FP + TN} \tag{4}$$

For a good classifier, TPR should be close to 1 while FPR should be close to 0.

III. RESULTS AND DISCUSSION

A. SPECTRAL PROFILE

In order to reveal the differences of the reflectance spectra between healthy and subtly bruised winter jujubes more intuitively, the average spectra with standard deviation (SD) of calibration set for four geographical origins of winter jujubes were calculated and presented in Figures 3 and 4. Figure 3 shows the average reflectance spectra of winter jujubes from four geographical origins acquired by NIR hyperspectral imaging system, whereas Figure 4 presents the data acquired by Vis-NIR hyperspectral imaging system.

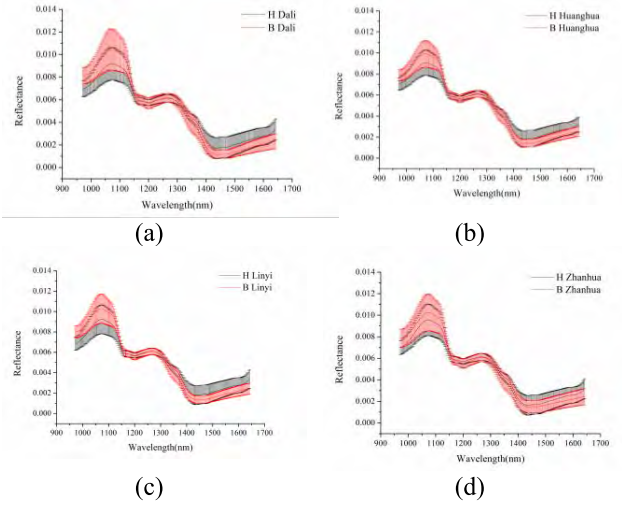

FIGURE 3. The average spectra with SD of four geographical origins of winter jujubes from four geographical origins acquired by NIR hyperspectral imaging system (H: Healthy; B: Bruised): (a) Dali winter jujube; (b) Huanghua winter jujube; (c) Linyi winter jujube; (d) Zhanhua winter jujube.

It can be seen from Figures 3 and 4, the variation trend of reflectance spectra curves of four geographical origins of winter jujubes is similar. In addition, healthy winter jujubes and subtly bruised samples also have similar variation trend of curves within one figure.

For NIR hyperspectral images, the spectral reflectance of bruised winter jujubes was slightly higher than that of healthy samples in the wavelength range of 972-1150 nm, whereas the average spectra of healthy samples were higher than bruised winter jujubes around 1400-1642 nm. As for the Vis-NIR hyperspectral images, the curve had the most obvious difference in the range of 569-688 nm and 753-947 nm. Although there are some differences in the spectra reflectance in specific spectra range, overlap still exists between two curves to some extent. So it is necessary to conduct further study in order to make a better distinction between healthy and bruised samples.

B. PIXEL-WISE PCA SCORE IMAGES

NIR hyperspectral images and Vis-NIR hyperspectral images of winter jujubes of single geographical origin were selected randomly to conduct PCA for quantitative analyses. More

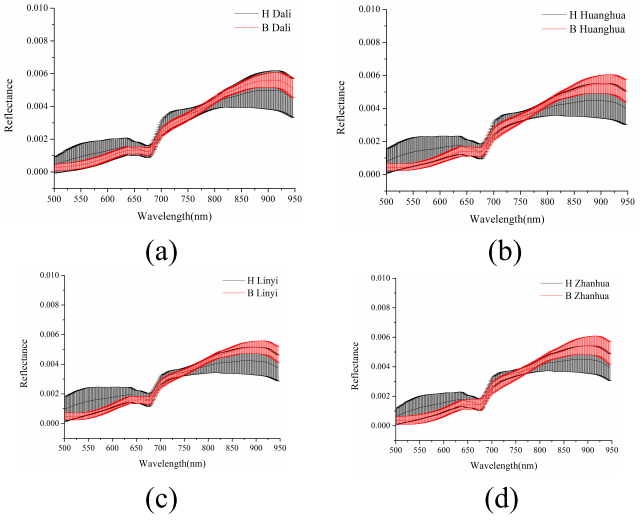

FIGURE 4. The average spectra with SD of winter jujubes from four geographical origins acquired by Vis-NIR hyperspectral imaging system (H: Healthy; B: Bruised): (a) Dali winter jujube; (b) Huanghua winter jujube; (c) Linyi winter jujube; (d) Zhanhua winter jujube.

than 99% of information in the original spectra was included in the first six PCs. Score images of the Dali winter jujube were shown in Figure 5. PCA score images of the other three geographical origins of winter jujubes were similar to those of the Dali winter jujube. Considering the size of image, PCA score images of the other three geographical origins of winter jujube were shown in Figures S1, S2 and S3 of the Supplementary Materials, respectively.

For NIR hyperspectral images, score image of PC3 shows obvious difference between healthy samples (blue color) and bruised winter jujubes (red color). Score images of PC5 and PC6 contained most of the noise information. For Vis-NIR hyperspectral image, the existence of staggered green and browning patches on the surface of winter jujubes brings difficulties for the classification of healthy and bruised samples. So discriminant models of both NIR and Vis-NIR hyperspectral images were needed to obtain better results.

C. DISCRIMINATION RESULTS OF DIFFERENT MODELS

SVM, LR and CNN models based on single geographical origin or all geographical origins of winter jujubes using pixel-wise spectra were built for quantitative analyses. The results are shown in Tables 1-6.

SVM and LR models based on single geographical origin or all geographical origins using NIR spectra (extracted from NIR hyperspectral images) all obtained decent results for healthy and bruised samples, with accuracies close to 100%, TPR close to 1 and FPR close to 0 for both calibration set and prediction set. The performance of the CNN model based on single geographical origin using NIR spectra were inferior to SVM and LR models, with accuracies surpassing 96% for calibration sets and accuracy in the range of 87%-100% for prediction sets. CNN model based on all geographical origins

TABLE 1. The classification accuracy of SVM models based on single geographical origin.

Spectra	Sample Origin [a]	Par. [b]		Cal. [c]				Pre. [d]				
		g [e]	c [f]	Pix. [g]	Acc. [h](%)	TPR [i]	FPR [j]	Com. [k] (s)	Pix.	Acc.(%)	TPR	FPR	Com. (s)
NIR	H.DL	1000	100	7133	99.99	1.00	0.00	0.89	2854	100.00	1.00	0.00	0.30
	B.DL			5075	99.98				2332	99.61			
	H.HH	1000	100	9826	99.45	0.99	0.00	4.24	3160	99.81	1.00	0.00	0.90
	B.HH			7479	99.85				2391	99.83			
	H.LY	1000	100	7463	100.00	1.00	0.00	0.80	3326	100.00	1.00	0.00	0.71
	B.LY			5844	100.00				2162	100.00			
	H.ZH.	1000	100	5850	100.00	1.00	0.00	0.85	1591	100.00	1.00	0.00	0.14
	B.ZH.			5596	100.00				1587	99.87			
Vis-NIR	H.DL	1000	100	51622	95.39	0.95	0.03	1212.10	13424	92.64	0.93	0.46	150.75
	B.DL			36158	97.48				13082	54.34			
	H.HH	1000	100	65481	95.70	0.96	0.01	1393.60	13515	97.49	0.97	0.26	147.07
	B.HH			50344	99.36				13674	73.94			
	H.LY	1000	100	49834	97.43	0.97	0.00	556.34	26416	98.46	0.98	0.31	124.57
	B.LY			38969	99.58				18857	68.89			
	H.ZH.	1000	100	43036	97.04	0.97	0.01	839.83	18198	98.53	0.99	0.67	101.54
	B.ZH.			38953	98.63				12380	32.97			

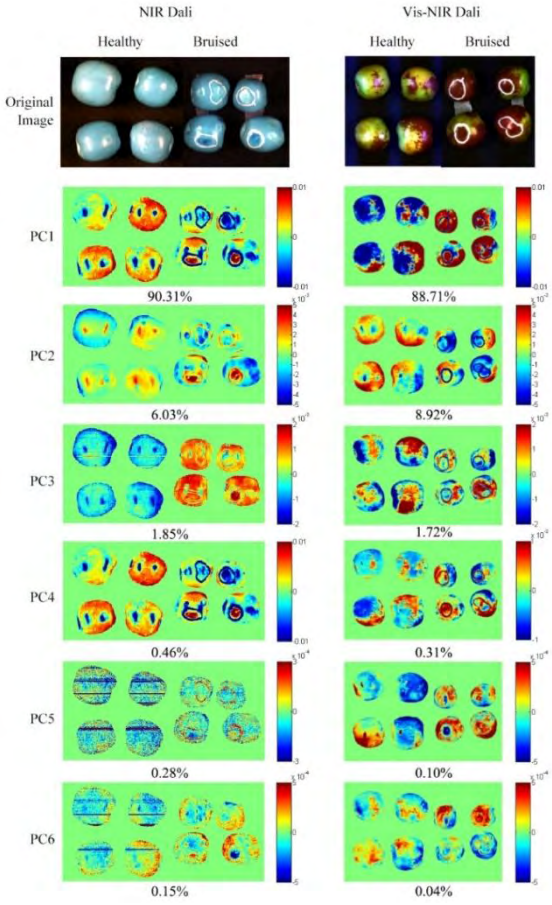

FIGURE 5. Score images for the first six principal components of dali winter jujube.

obtained satisfactory results, with all accuracies over 94%, TPRs reaching 1 and FPRs close to 0.

The performances of SVM and CNN models based on single geographical origin using Vis-NIR spectra (extracted from Vis-NIR hyperspectral images) were inferior to LR models. The FPR of Dali and Zhanhua winter jujubes were higher than 0.4. Among all the three models based on all geographical origins using Vis-NIR spectra, the CNN model had the best performance with the most of accuracies surpassing 70% of prediction set. Moreover, the TPRs reached 0.90, 0.93 for calibration set and prediction set, respectively. The FPR of CNN model were also lower than SVM and LR models.

Compared with healthy winter jujubes, bruised samples showed lower classification accuracies for SVM and LR models using Vis-NIR spectra, especially for bruised Dali winter jujube and Zhanhua winter jujube. Different from SVM and LR models, the CNN model based on all geographical origins using Vis-NIR spectra achieved reasonable results for the subtle bruises detection of Huanghua and Linyi winter jujube, with accuracies reaching more than 90%.

On the whole, green and browning patches of winter jujubes made it difficult to discriminate bruised samples from healthy winter jujubes using Vis-NIR spectra due to the fact that Vis-NIR spectra were sensitive to color information. SVM, LR, CNN models using NIR spectra performed much better than models using Vis-NIR spectra, with most accuracies close to 100%.

In addition, the Huanghua and Linyi winter jujubes got better performances in the discrimination of bruised samples using Vis-NIR spectra than Dali and Zhanhua winter jujubes. The results of models using samples from all geographical origins were close to those using samples from single geographical origin. The results also showed that winter jujubes from different origins also had an influence on the results.

The performances of the models were also compared from the perspective of computation time. For NIR spectra, modelling of CNN takes more time and SVM takes the least amount of time. Furthermore, the prediction of three models were fast, and the computation time of the CNN prediction set was at an intermediate level among the three models. For Vis-NIR spectra, SVM models would spend more time for model establishment and prediction while LR models took

TABLE 2. The classification accuracy of SVM model based on all geographical origins.

Spectra	Sample Origin	Par.		Cal.					Pre.				
		g	c	Pix.	Acc.(%)	TPR	FPR	Com. (s)	Pix.	Acc.(%)	TPR	FPR	Com.(s)
NIR	H.DL	1000	100	7133	99.97	1.00	0.00	33.17	2854	100.00	1.00	0.00	7.25
	B.DL			5075	99.55				2332	99.70			
	H.HH			9826	98.58				3160	99.62			
	B.HH			7479	99.96				2391	100.00			
	H.LY			7463	100.00				3326	100.00			
	B.LY			5844	99.86				2162	99.53			
	H.ZH.			5850	100.00				1591	100.00			
	B.ZH.			5596	99.54				1587	98.54			
	Totol			54266					19403				
Vis-NIR	H.DL	1000	100	51622	93.95	0.94	0.03	27848.00	13424	93.39	0.96	0.30	3281.61
	B.DL			36158	93.60				13082	64.01			
	H.HH			65481	93.69				13515	95.31			
	B.HH			50344	98.91				13674	89.54			
	H.LY			49834	94.42				26416	97.19			
	B.LY			38969	99.39				18857	86.50			
	H.ZH.			43036	95.94				18198	98.13			
	B.ZH.			38953	95.73				12380	29.22			
	Totol			374397					129546				

TABLE 3. The classification accuracy of LR models based on single geographical origin.

Spectra	Sample Origin	Cal.					Pre.				
		Pix.	Acc. (%)	TPR	FPR	Com. (s)	Pix.	Acc. (%)	TPR	FPR	Com. (s)
NIR	H.DL	7133	100.00	1.00	0.00	3.33	2854	99.33	0.99	0.01	0.02
	B.DL	5075	100.00				2332	99.40			
	H.HH	9826	99.67	1.00	0.01	11.46	3160	98.86	0.99	0.00	0.02
	B.HH	7479	99.37				2391	99.54			
	H.LY	7463	100.00	1.00	0.00	9.44	3326	99.70	1.00	0.00	0.02
	B.LY	5844	100.00				2162	99.96			
	H.ZH.	5850	100.00	1.00	0.00	3.84	1591	98.30	0.98	0.00	0.03
	B.ZH.	5596	100.00				1587	99.56			
Vis-NIR	H.DL	51622	86.60	0.87	0.15	17.16	13424	89.81	0.90	0.35	0.27
	B.DL	36158	84.81				13082	65.46			
	H.HH	65481	89.15	0.89	0.08	21.75	13515	90.52	0.91	0.17	0.30
	B.HH	50344	91.86				13674	83.01			
	H.LY	49834	91.84	0.92	0.05	21.75	26416	94.75	0.95	0.20	0.31
	B.LY	38969	94.63				18857	79.56			
	H.ZH.	43036	87.53	0.88	0.10	3.84	18198	92.77	0.93	0.43	0.26
	B.ZH.	38953	90.05				12380	57.46			

the shortest time. The prediction time of models using NIR spectra and Vis-NIR spectra showed that these models had the great potential for real time detection. It should be noted that the computation time of prediction set is more important for realistic application once the models are built.

In order to compare the performance of CNN and the other two models more intuitively, the color of per grid in Figure 6 reveals the difference of modelling results. The warmer the color for per grid is, the better classification accuracy obtained by CNN model was. Compared with SVM model, CNN model performed better for models using Vis-NIR spectra, whereas the results of CNN models built according to NIR spectra were close to the results of SVM models. The results of CNN models were also close to LR models with the most of the differences between two models were −5%-5%.

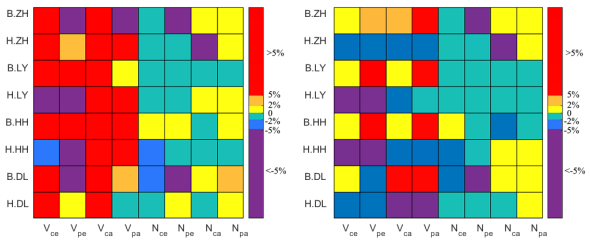

FIGURE 6. Difference maps of accuracy between CNN and the other model (Vce, Vpa, Nce and Npa represent for calibration set of model based on single geographical origin using Vis-NIR spectra, prediction set of model based on all geographical origins using Vis-NIR spectra, calibration set of model based on single geographical origin using NIR spectra, prediction set of model based on all geographical origins using NIR spectra, respectively.): (a) CNN-SVM; (b) CNN-LR.

D. PREDICTION MAPS

In order to reveal the classification results of CNN model more intuitively, prediction maps based on CNN model based on all geographical origins were are shown in Figure 7. It can be seen from Figure 7, CNN model using NIR spectra was more distinguishable for healthy and bruised samples.

TABLE 4. The classification accuracy of LR model based on all geographical origins.

Spectra	SampleOrigin	Cal.					Pre.				
		Pix.	Acc.(%)	TPR	FPR	Com.(s)	Pix.	Acc.(%)	TPR	FPR	Com.(s)
NIR	H.DL	7133	99.96	1.00	0.01	42.39	2854	99.97	1.00	0.01	0.37
	B.DL	5075	98.54				2332	96.83			
	H.HH	9826	99.99				3160	99.97			
	B.HH	7479	99.50				2391	99.26			
	H.LY	7463	98.26				3326	99.75			
	B.LY	5844	99.93				2162	100.00			
	H.ZH.	5850	100.00				1591	100.00			
	B.ZH.	5596	98.91				1587	97.78			
	Total	54266					19403				
Vis-NIR	H.DL	51622	81.63	0.84	0.12	109.06	13424	85.07	0.88	0.22	1.05
	B.DL	36158	80.24				13082	66.40			
	H.HH	65481	84.88				13515	85.71			
	B.HH	50344	91.53				13674	89.04			
	H.LY	49834	84.98				26416	88.61			
	B.LY	38969	94.41				18857	90.29			
	H.ZH.	43036	84.45				18198	90.99			
	B.ZH.	38953	83.18				12380	59.87			
	Total	374397					129546				

TABLE 5. The classification accuracy of CNN models based on single geographical origin.

Spectra	SampleOrigin	Par.			Cal.				Val.				Pre.		
		B.S.[b]	T.E.[c]	T.I.[d]	Pix.	Acc.(%)	TPR	FPR	Com.(s)	Pix.	Acc.(%)	Pix.	Acc.(%)	TPR	FPR	Com.(s)
NIR	H.DL	500	32	0.01	7133	99.93	1.00	0.02	22.40	2832	99.86	2854	99.51	1.00	0.13	0.14
	B.DL				5075	98.03				1895	96.57	2332	87.09			
	H.HH	500	30	0.01	9826	96.96	0.97	0.00	27.00	2983	98.29	3160	98.51	0.99	0.00	0.18
	B.HH				7479	99.85				2122	98.40	2391	99.67			
	H.LY	500	30	0.01	7463	99.87	1.00	0.00	21.00	2451	99.80	3326	99.40	0.99	0.00	0.16
	B.LY				5844	99.86				2122	99.25	2162	99.84			
	H.ZH.	500	40	0.01	5850	99.81	1.00	0.00	24.00	2458	99.84	1591	98.24	0.98	0.08	0.15
	B.ZH.				5596	99.54				1639	93.65	1587	92.14			
Vis-NIR	H.DL	300	14	0.01	51622	93.29	0.93	0.01	240.23	14474	92.17	13424	90.18	0.90	0.48	2.15
	B.DL				36158	98.83				11279	55.60	13082	52.26			
	H.HH	500	22	0.01	65481	89.09	0.89	0.00	585.75	22211	87.62	13515	84.26	0.84	0.04	1.92
	B.HH				50344	99.98				16943	98.26	13674	96.23			
	H.LY	500	22	0.01	49834	85.98	0.86	0.00	475.52	23421	83.68	26416	88.03	0.88	0.05	1.58
	B.LY				38969	99.92				16906	94.57	18857	95.31			
	H.ZH.	500	30	0.01	43036	93.86	0.94	0.00	447.33	16739	94.53	18198	96.54	0.97	0.62	1.34
	B.ZH.				38953	99.56				14078	24.41	12380	37.62			

TABLE 6. The classification accuracy of CNN model based on all geographical origins.

Spectra	Sample Origin	Par.			Cal.					Val.				Pre.		
		B.S.	T.E.	T.I.	Pix.	Acc.(%)	TPR	FPR	Com.(s)	Pix.	Acc.(%)	Pix.	Acc.(%)	TPR	FPR	Com.(s)
NIR	H.DL	800	38	0.01	7133	99.94	1.00	0.02	98.80	2832	99.23	2854	100.00	1.00	0.00	0.59
	B.DL				5075	99.88				1895	100.00	2332	99.77			
	H.HH				9826	99.96				2983	99.08	3160	99.97			
	B.HH				7479	97.94				2122	100.00	2391	99.66			
	H.LY				7463	99.86				2451	99.96	3326	99.96			
	B.LY				5844	99.61				2122	99.95	2162	99.08			
	H.ZH.				5850	94.82				2458	99.92	1591	100.00			
	B.ZH.				5596	99.97				1639	99.76	1587	99.62			
	Total				54266					18502		19403				
Vis-NIR	H.DL	800	30	0.01	51622	86.95	0.90	0.01	3271.80	14474	92.05	13424	84.70	0.93	0.24	6.37
	B.DL				36158	98.38				11279	72.04	13082	70.63			
	H.HH				65481	90.15				22211	91.93	13515	90.72			
	B.HH				50344	99.67				16943	98.13	13674	94.71			
	H.LY				49834	92.25				23421	89.12	26416	96.25			
	B.LY				38969	99.92				16906	81.75	18857	91.79			
	H.ZH.				43036	92.21				16739	93.32	18198	95.91			
	B.ZH.				38953	98.77				14078	17.89	12380	39.27			
	Total				374397					136051		129546				

For prediction map using Vis-NIR spectra, Huanghua winter jujube and Linyi winter jujube achieved reasonable discrimination results contrast with the other two geographical origins of winter jujube. For Vis-NIR hyperspectral images, the predicted bruised regions were not the entire region. Specially, the marked regions in the Vis-NIR hyperspectral

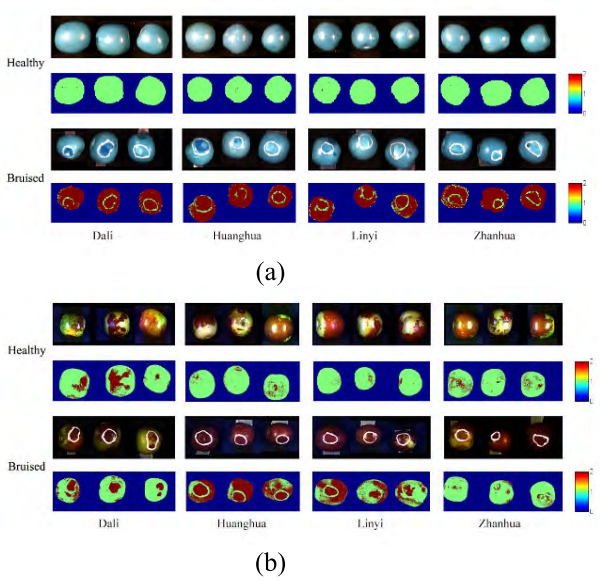

FIGURE 7. Prediction maps based on CNN model based on all geographical origins: (a) Prediction map using NIR spectra; (b) Prediction map using Vis-NIR spectra.

images can be identified. Some other regions were also predicted as bruised, the reason might be that only one bruised region was marked, and there might be more bruised regions within the bruised samples. As shown in Figures 1 and 7, color differences could be found within one sample, and the reflectance spectra could be influenced by the different distribution of color in the Vis-NIR region. Another factor of winter jujubes was that the bruised region had the similar color of those healthy regions (browning), which resulted in the difficulties of identifying healthy and bruised pixels. Thus, the results of healthy pixels were also influenced by the color information. The prediction maps of winter jujubes in the Vis-NIR image were influenced by the color distribution. It was also noted that for NIR hyperspectral images, the entire sample region except the marked circles of the bruised jujubes were predicted as bruised. This might be caused by the unique characteristic of winter jujubes that the winter jujubes deteriorated rapidly, and the chemical composition changed after damaging. The NIR region related more to the chemical compositions, thus the healthy samples in the NIR hyperspectral images were predicted with nearly 100% prediction accuracy. The reason might be that the bruised winter jujubes deteriorated rapidly, and the chemical composition changed after damaging.

IV. CONCLUSIONS

In this study, pixel-wise NIR spectra and Vis-NIR spectra were both applied to detect subtle bruises on winter jujubes. Pixel-wise spectra could extend the amount of data and covered much more details compared with average spectra of samples. The results proved the feasibility of using pixel-wise spectra extracted from hyperspectral images to detect subtle bruises on winter jujubes.

As one of the widely used deep learning methods, CNN has showed great potential for data analyses in various fields. In this study, SVM, LR and CNN models built on single geographical origin or all geographical origins were compared. TPR and FPR were employed to compare the efficiency of the models. SVM, LR and CNN models using NIR spectra all obtained decent results with accuracies close to 100%, TPRs and FPRs close to 1 and 0, respectively. For Vis-NIR spectra, the results of CNN models were better than those of SVM models. Compared with LR models, CNN models performed better in the discrimination of bruised samples. Models using NIR spectra performed better than models based on Vis-NIR, and the reason might be that NIR spectra related to chemical changes while Vis-NIR spectra were likely to be interfered by factors such as the color of winter jujubes. Among three models, CNN were more effective to extract features using Vis-NIR spectra which had many interference factors.

Moreover, the modelling time and prediction time were also used to evaluate the performance of models. The time efficiency of CNN models was at an intermediate level among three models. On the whole, the results of CNN models were close to those of SVM and LR models, indicting the feasibility of CNN to detect subtle bruises on winter jujubes using hyperspectral images.

The results of the detection of bruised winter jujubes from different geographical origins were different, indicating that the geographical origin variations had influence on the detection performances. The performances of models using samples from a single geographical origin and all geographical origins indicted that models covering more geographical origins would benefit the bruise detection. In this study, only 75 healthy jujubes and 75 bruised jujubes of each geographical origin were prepared. In the future study, the number of samples should be expanded to improve the universality of the CNN model. Besides, the spatial information of samples should also be included and utilized to improve the performances of CNN models.

APPENDIX

Figure S1: Score images for the first six principal components of Huanghua winter jujube.

Figure S2: Score images for the first six principal components of Linyi winter jujube.

Figure S3: Score images for the first six principal components of Zhanhua winter jujube.

REFERENCES

[1] X. Kou, Y. He, Y. Li, X. Chen, Y. Feng, and Z. Xue, "Effect of abscisic acid (ABA) and chitosan/nano-silica/sodium alginate composite film on the color development and quality of postharvest Chinese winter jujube (*Zizyphus jujuba* Mill. cv. Dongzao)," *Food Chem.*, vol. 270, pp. 385–394, Jan. 2019.

[2] N. N. Mohsenin, "Physical properties of plant and animial materials: Structure, physical characterisitics and mechanical properties," *J. Biomed. Mater. Res. B, Appl. Biomater.*, vol. 11, no. 1, pp. 83–89, 1968.

[3] M. A. Cox, M. I. N. Zhang, and J. H. M. Willison, "Apple bruise assessment through electrical impedance measurements," *J. Pomology Horticultural Sci.*, vol. 68, no. 3, pp. 393–398, 1993.

[4] H. Zhang, J. Wang, and S. Ye, "Predictions of acidity, soluble solids and firmness of pear using electronic nose technique," *J. Food Eng.*, vol. 86, no. 3, pp. 370–378, 2008.
[5] Q. Yang, "An approach to apple surface feature detection by machine vision," *Comput. Electron. Agricult.*, vol. 11, pp. 249–264, Nov. 1994.
[6] Z. Wen and Y. Tao, "Building a rule-based machine-vision system for defect inspection on apple sorting and packing lines," *Expert Syst. Appl.*, vol. 16, pp. 307–313, Apr. 1999.
[7] A. Ambrose, L. M. Kandpal, M. S. Kim, W.-H. Lee, and B.-K. Cho, "High speed measurement of corn seed viability using hyperspectral imaging," *Infr. Phys. Technol.*, vol. 75, pp. 173–179, Mar. 2016.
[8] L. M. Kandpal, S. Lohumi, M. S. Kim, J.-S. Kang, and B.-K. Cho, "Near-infrared hyperspectral imaging system coupled with multivariate methods to predict viability and vigor in muskmelon seeds," *Sens. Actuators B., Chem.*, vol. 229, pp. 534–544, Jun. 2016.
[9] C. Zhang, Q. Wang, F. Liu, Y. He, and Y. Xiao, "Rapid and non-destructive measurement of spinach pigments content during storage using hyperspectral imaging with chemometrics," *Measurement*, vol. 97, pp. 149–155, Feb. 2017.
[10] G. Lu and B. Fei, "Medical hyperspectral imaging: A review," *J. Biomed. Opt.*, vol. 19, no. 1, p. 10901, Jan. 2014.
[11] C. Liu, W. Liu, X. Lu, W. Chen, J. Yang, and L. Zheng, "Nondestructive determination of transgenic Bacillus thuringiensis rice seeds (Oryza sativa L.) using multispectral imaging and chemometric methods," *Food Chem.*, vol. 153, pp. 87–93, Jun. 2014.
[12] C. Zhang, F. Liu, W. Kong, and Y. He, "Application of visible and near-infrared hyperspectral imaging to determine soluble protein content in oilseed rape leaves," *Sensors*, vol. 15, no. 7, pp. 16576–16588, 2015.
[13] P. Baranowski, W. Mazurek, J. Wozniak, and U. Majewska, "Detection of early bruises in apples using hyperspectral data and thermal imaging," *J. Food Eng.*, vol. 110, pp. 345–355, Jun. 2012.
[14] J. Zhao, O. Qin, Q. Chen, and J. Wang, "Detection of bruise on pear by hyperspectral imaging sensor with different classification algorithms," *Sensor Lett.*, vol. 8, no. 4, pp. 570–576, 2010.
[15] S. Fan, C. Li, W. Huang, and L. Chen, "Detection of blueberry internal bruising over time using NIR hyperspectral reflectance imaging with optimum wavelengths," *Postharvest Biol. Technol.*, vol. 134, pp. 55–66, Dec. 2017.
[16] S. Fan, C. Li, W. Huang, and L. Chen, "Data fusion of two hyperspectral imaging systems with complementary spectral sensing ranges for blueberry bruising detection," *Sensors*, vol. 18, no. 12, p. E4463, 2018.
[17] G. Elmasry, N. Wang, C. Vigneault, J. Qiao, and A. Elsayed, "Early detection of apple bruises on different background colors using hyperspectral imaging," *LWT-Food Sci. Technol.*, vol. 41, no. 2, pp. 337–345, 2008.
[18] D. P. Ariana, R. Lu, and D. E. Guyer, "Near-infrared hyperspectral reflectance imaging for detection of bruises on pickling cucumbers," *Comput. Electron. Agricult.*, vol. 53, no. 1, pp. 60–70, 2006.
[19] J. Qin, T. F. Burks, M. A. Ritenour, and W. G. Bonn, "Detection of citrus canker using hyperspectral reflectance imaging with spectral information divergence," *J. Food Eng.*, vol. 93, no. 2, pp. 183–191, 2009.
[20] D. Ye, L. Sun, W. Tan, W. Che, and M. Yang, "Detecting and classifying minor bruised potato based on hyperspectral imaging," *Chemometrics Intell. Lab. Syst.*, vol. 177, pp. 129–139, Jun. 2018.
[21] C. Zhang, F. Liu, and Y. He, "Identification of coffee bean varieties using hyperspectral imaging: Influence of preprocessing methods and pixel-wise spectra analysis," *Sci. Rep.*, vol. 8, Feb. 2018, Art. no. 2166.
[22] O. Matsuda *et al.*, "Determination of seed soundness in conifers *cryptomeria japonica and chamaecyparis obtusa* using narrow-multiband spectral imaging in the short-wavelength infrared range," *PLoS ONE*, vol. 10, no. 6, 2015, Art. no. e0128358.
[23] Y. Zhao, S. Zhu, Z. Chu, X. Feng, F. Lei, and H. Yong, "Application of hyperspectral imaging and chemometrics for variety classification of maize seeds," *RSC Adv.*, vol. 8, pp. 1337–1345, Jan. 2018.
[24] J. Sun, X. Lu, H. Mao, X. Jin, and X. Wu, "A method for rapid identification of rice origin by hyperspectral imaging technology," *J. Food Process Eng.*, vol. 40, no. 1, 2017, Art. no. e12297.
[25] L. Feng, S. Zhu, C. Zhang, Y. Bao, P. Gao, and L. He, "Variety identification of raisins using near-infrared hyperspectral imaging," vol. 23, no. 11, p. 2907, 2018.
[26] W. Che *et al.*, "Pixel based bruise region extraction of apple using Vis-NIR hyperspectral imaging," *Comput. Electron. Agricult.*, vol. 146, pp. 12–21, Mar. 2018.
[27] H. Petersson, D. Gustafsson, and D. Bergström, "Hyperspectral image analysis using deep learning—A review," in *Proc. 6th Int. Conf. Image Process. Theory, Tools Appl.*, Dec. 2017, pp. 1–6.
[28] E. Aptoula, M. C. Ozdemir, and B. Yanikoglu, "Deep learning with attribute profiles for hyperspectral image classification," *IEEE Geosci. Remote Sens. Lett.*, vol. 13, no. 12, pp. 1970–1974, Dec. 2016.
[29] X. Yu, H. Lu, and Q. Liu, "Deep-learning-based regression model and hyperspectral imaging for rapid detection of nitrogen concentration in oilseed rape (*Brassica napus* L.) leaf," *Chemometrics Intell. Lab. Syst.*, vol. 172, pp. 188–193, Jan. 2017.
[30] J. Yue, S. Mao, and M. Li, "A deep learning framework for hyperspectral image classification using spatial pyramid pooling," *Remote Sens. Lett.*, vol. 7, no. 9, pp. 875–884, 2016.
[31] S. Sumriddetchkajorn and Y. Intaravanne, "Hyperspectral imaging-based credit card verifier structure with adaptive learning," *Appl. Opt.*, vol. 47, no. 35, pp. 6594–6600, 2008.
[32] Q. Liu, F. Zhou, R. Hang, and X. Yuan, "Bidirectional-convolutional LSTM based spectral-spatial feature learning for hyperspectral image classification," *Remote Sens.*, vol. 9, no. 12, p. 1330, 2017.
[33] J. Li, L. Bruzzone, and S. Liu, "Deep feature representation for hyperspectral image classification," in *Proc. IEEE Int. Geosci. Remote Sens. Symp. (IGARSS)*, Jul. 2015, pp. 4951–4954.
[34] J. Yue, W. Zhao, S. Mao, and H. Liu, "Spectral-spatial classification of hyperspectral images using deep convolutional neural networks," *Remote Sens. Lett.*, vol. 6, no. 6, pp. 468–477, May 2015.
[35] A. Mughees and L. Tao, "Efficient deep auto-encoder learning for the classification of hyperspectral images," in *Proc. Int. Conf. Virtual Reality Vis. (ICVRV)*, Sep. 2016, pp. 44–51.
[36] J. Acquarelli, T. van Laarhoven, J. Gerretzen, T. N. Tran, L. M. C. Buydens, and E. Marchiori, "Convolutional neural networks for vibrational spectroscopic data analysis," *Analytica Chim. Acta*, vol. 954, pp. 22–31, Feb. 2017.
[37] J. Liu, M. Osadchy, L. Ashton, M. Foster, C. J. Solomon, and S. J. Gibson, "Deep convolutional neural networks for Raman spectrum recognition: A unified solution," *Analyst*, vol. 142, no. 21, pp. 4067–4074, 2017.
[38] Z. Qiu, J. Chen, Y. Zhao, S. Zhu, Y. He, and C. Zhang, "Variety identification of single rice seed using hyperspectral imaging combined with convolutional neural network," *Appl. Sci.*, vol. 8, no. 2, p. 212, 2018.
[39] X. Yu, L. Tang, X. Wu, and H. Lu, "Nondestructive freshness discriminating of shrimp using visible/near-infrared hyperspectral imaging technique and deep learning algorithm," *Food Anal. Methods*, vol. 11, no. 3, pp. 768–780, 2018.
[40] C. Mcgoverin and M. Manley, "Classification of maize kernel hardness using near infrared hyperspectral imaging," *J. Near Infr. Spectrosc.*, vol. 20, no. 5, pp. 529–535, 2012.
[41] W. Lu, H. Pu, D.-W. Sun, L. Dan, Q. Wang, and Z. Xiong, "Application of hyperspectral imaging for prediction of textural properties of maize seeds with different storage periods," *Food Anal. Methods*, vol. 8, pp. 1535–1545, Jul. 2015.
[42] J. He, C. Zhang, and Y. He, "Application of near-infrared hyperspectral imaging to detect sulfur dioxide residual in the *Fritillaria thunbergii* bulbus treated by sulfur fumigation," *Appl. Sci.*, vol. 7, no. 1, p. 77, 2017.
[43] L. Feng, S. Zhu, C. Zhang, Y. Bao, X. Feng, and L. He, "Identification of maize kernel vigor under different accelerated aging times using hyperspectral imaging," vol. 23, no. 12, p. 3078, 2018.
[44] D. Liu *et al.*, "Prediction of color and pH of salted porcine meats using visible and near-infrared hyperspectral imaging," *Food Bioprocess Technol.*, vol. 7, pp. 3100–3108, Nov. 2014.
[45] C. Zhang, X. Feng, J. Wang, F. Liu, L. He, and W. Zhou, "Mid-infrared spectroscopy combined with chemometrics to detect Sclerotinia stem rot on oilseed rape (*Brassica napus* L.) leaves," vol. 13, p. 39, May 2017.
[46] B.-C. Kuo, H.-H. Ho, C.-H. Li, C.-C. Hung, and J.-S. Taur, "A kernel-based feature selection method for SVM with RBF kernel for hyperspectral image classification," *IEEE J. Sel. Topics Appl. Earth Observ. Remote Sens.*, vol. 7, no. 1, pp. 317–326, Jan. 2014.
[47] M. Pal and P. M. Mather, "Assessment of the effectiveness of support vector machines for hyperspectral data," *Future Gener. Comput. Syst.*, vol. 20, no. 7, pp. 1215–1225, 2004.
[48] R. Archibald and G. Fann, "Feature selection and classification of hyperspectral images with support vector machines," *IEEE Geosci. Remote Sens. Lett.*, vol. 4, no. 4, pp. 674–677, Oct. 2007.
[49] N. Wu, C. Zhang, X. Bai, X. Du, and Y. He, "Discrimination of *Chrysanthemum* varieties using hyperspectral imaging combined with a deep convolutional neural network," *Molecules*, vol. 23, no. 11, p. 2831, 2018.

[50] X. Zhang, T. Lin, J. Xu, X. Luo, and Y. Ying, "DeepSpectra: An end-to-end deep learning approach for quantitative spectral analysis," *Analytica Chim. Acta*, vol. 1058, pp. 48–57, Jun. 2019.
[51] T. Oshea and J. Hoydis, "An introduction to deep learning for the physical layer," *IEEE Trans. Cogn. Commun. Netw.*, vol. 3, no. 4, pp. 563–575, 2017.
[52] T. Fawcett, "ROC graphs: Notes and practical considerations for researchers," *Mach. Learn.*, vol. 31, no. 1, pp. 1–38, 2004.

LEI FENG received the B.S. degree in agricultural engineering from Zhejiang Agricultural University, Hangzhou, China, in 1991, and the M.S. and Ph.D. degrees in agricultural engineering from Zhejiang University, Hangzhou, in 1999 and 2005, respectively, where he is currently an Associate Professor.

SUSU ZHU received the B.S. degree in biosystems engineering from the College of Biosystems Engineering and Food Science, Zhejiang University, Hangzhou, China, in 2017, where she is currently pursuing the master's degree with the College of Biosystems Engineering and Food Science. She currently works on her thesis in the agricultural field using the hyperspectral imaging technology.

LEI ZHOU received the B.S. degree in automation from the School of Technology, Beijing Forestry University, Beijing, China, in 2017. He is currently pursuing the Ph.D. degree with the College of Biosystems Engineering and Food Science, Zhejiang University. His research interests include the deep learning in the agriculture and the agricultural Internet of Things.

YIYING ZHAO received the B.S. degree in biosystems engineering from the College of Biosystems Engineering and Food Science, Zhejiang University, Hangzhou, China, in 2016, where she is currently pursuing the Ph.D. degree with the College of Biosystems Engineering and Food Science. Her research interest includes the spectroscopic imaging analysis and its application in the disease detection in agriculture.

YIDAN BAO received the B.E. degree in electrical engineering from Zhejiang University, Hangzhou, China, in 1984, the M.S. degree in agricultural engineering from Zhejiang Agricultural University, Hangzhou, in 1993, and the Ph.D. degree in agricultural engineering from Zhejiang University, in 2013.

She is currently an Associate Professor with Zhejiang University.

CHU ZHANG received the B.S. degree in electronic and information engineering from Northwest A&F University, Yangling, China, in 2011, and the Ph.D. degree in agricultural electrification and automation from the College of Biosystems Engineering and Food Science, Zhejiang University, Hangzhou, China, in 2016, where he is currently holding a postdoctoral position with the College of Biosystems Engineering and Food Science. His research interests include the spectroscopy and spectral imaging analysis, and the application in the agriculture and food.

YONG HE received the B.S. and M.S. degrees in agricultural engineering from Zhejiang Agricultural University, Hangzhou, China, in 1984 and 1987, respectively, and the Ph.D. degree in biosystems engineering from Zhejiang University, Hangzhou, in 1998, where he is currently a Professor. He is currently the Dean of the College of Biosystems Engineering and Food Science, Zhejiang University, the Director of the Key Laboratory of Spectroscopy, Ministry of Agriculture, the national prestigious teacher, and one of the hundred thousands of national talents. He was selected as the Clarivate Analytics Global Highly Cited Researchers (2016–2018). He is the Editor-in-Chief of the *Computers and Electronics in Agriculture* and the editorial board member of the *Food and Bioprocess Technology*.